MID-INFRARED (8–21 MICRON) IMAGING OF PROTO–PLANETARY NEBULAE

ADITYA DAYAL,[1] WILLIAM F. HOFFMANN, AND JOHN H. BIEGING
Steward Observatory, University of Arizona, Tucson, AZ 85721

JOSEPH L. HORA
Institute for Astronomy, 2680 Woodlawn Drive, Honolulu HI 96822

LYNNE K. DEUTSCH
Astronomy Department, Boston University, Boston, MA 02215

AND

GIOVANNI G. FAZIO
Center for Astrophysics, 60 Garden Street, Cambridge MA 02138

ABSTRACT

We present mid-infrared (8–21 μm) images of thermal dust emission from two proto–planetary nebulae (PPNs), IRAS 07134+1005 and IRAS 22272+5435, which show a strong 21 μm emission feature. Both of the sources are well resolved and show evidence for axial symmetry. From our images, we calculate temperature and optical depth maps and estimate the abundance of the 11 μm and 21 μm feature carriers. In both sources, the dust temperatures range from $\sim$160–200 K. The optical depths in IRAS 07134 are about a factor of 3 lower than those in IRAS 22272, but the emission is optically thin in both sources. Our analyses of the feature-to-continuum ratios suggests that 0.5%–5% of the carbon in these objects may be in the form of large PAH molecules. We construct optically thin, axially symmetric cylindrical shell models to simulate the observed mid-IR morphologies and spectra, and calculate nebular masses of 0.26 $M_{\odot}$ for IRAS 07134 and 0.42 $M_{\odot}$ for IRAS 22272. Although the mid-IR emission primarily comes from warm ($T \approx 190$ K) dust, our models require a significant cooler dust ($T \approx 80$ K) component to fit the observed mid- and far-IR spectral energy distributions.

Subject headings: dust, extinction — infrared: ISM: continuum — ISM: abundances — planetary nebulae: general

1. INTRODUCTION

Asymptotic giant branch (AGB) stars exhibit high rates of mass loss and dust grain formation as they evolve toward the planetary nebula (PN) phase. The development of a dusty circumstellar envelope leads to the gradual obscuration of the star at optical and ultraviolet wavelengths, and a corresponding increase in its infrared brightness. During this transitory process, there comes a point when a significant portion of the outer layers of the star have been ejected, leading to a decrease in the mass-loss rate, yet the photospheric temperature of the star is still not hot enough to ionize the circumstellar nebula ($T_{\rm star} \ll 30{,}000$ K). At this time, the circumstellar dust shell appears detached from the stellar photosphere, and the object is called a proto–planetary nebula (PPN). The spectral energy distributions (SEDs) of proto–planetary nebulae (PPNs) usually show two peaks: a peak in the optical, corresponding to emission from the central star, and a peak in the mid-IR, showing thermal emission from the detached dust shell (e.g. Kwok 1993). PPNs appear as bright infrared sources, reradiating most of their energy in the mid- (5–25 μm) and far- (25–200 μm) IR. High spatial resolution imaging of PPNs can provide information on the overall structure and morphology of the warm ($T \approx 200$ K) dust as well as on the spatial distribution of spectral emission features. Previous mid-IR imaging studies of PPNs indicate that most resolved sources are not spherically symmetric, but exhibit some

kind of axial symmetry (Meixner et al. 1997; Hora et al. 1996; Hawkins et al. 1995; Skinner et al. 1994), suggesting that asymmetries in the mass-loss process develop during or shortly after the star leaves the AGB.

In this paper, we present mid-IR images of 2 carbon-rich (C/O > 1) PPNs, IRAS 07134+1005 and IRAS 22272+5435 that were identified by Kwok, Volk, & Hrivnak (1989) as having prominent 21 μm emission features from their IRAS low-resolution spectra (LRS). Both of these sources have double-peaked SEDs and are associated with bright optical stars with spectra resembling F- and G-type supergiants (Hrivnak 1995; Hrivnak, Kwok, & Volk 1989). The mid-IR spectra (Justtanont et al. 1996; Buss et al. 1990) show that both of these sources have several emission features between 7–13 μm, superposed on broad emission plateaus. These features differ somewhat from the traditional unidentified (UIR) features at 3.3, 6.2, 7.7, 8.6, 11.3, and 12.7 μm, ascribed to polycyclic aromatic hydrocarbons (PAHs; Léger & Puget 1984; Allamandola, Tielens, & Barker 1989). These emission bands can, however, be fitted by laboratory spectra of various carbonaceous compounds, including simple PAH molecules (Justtanont et al. 1996) and coal grains (Guillois et al. 1996). Our 11.7 μm image samples emission from 11.5 and 12.2 μm emission bands, as well as the 11–13 μm emission plateau. As mentioned above, both of these sources show the "21 μm feature," a broad unidentified emission feature from 19–23 μm. The carrier of this feature has not been identified, but there is ample evidence for the carbon-rich nature of these sources (Bakker et al. 1996; Hrivnak 1995), so it is reasonable to assume that carbonaceous material may be responsible for

[1] Present address: JPL/Caltech, MS 183-900, 4800 Oak Grove Drive, Pasadena, CA 91109; adayal@lb6.jpl.nasa.gov.

the 21 μm emission feature. Our 20.6 μm broadband image samples emission from this broad 21 μm feature. We use our 11.7 and 20.6 μm images and others that sample the dust continuum to look for spatial differences between these spectrally distinct emitters. Both objects have been previously imaged by Meixner et al. (1997) in the 10 μm window using Berkcam. Our observations extend the study of these sources to 21 μm, with better spatial sampling and higher sensitivity.

Section 2 presents ground-based images of PPNs covering the range 8–21 μm. In § 3 we derive temperature and optical depth maps from our images, and calculate abundances of feature emitters from feature-to-continuum maps. In § 4, we construct simple geometrical models of our sources and show that the observed morphologies are consistent with optically thin, cylindrical dust shells. Finally, we present a discussion of our results in § 5 and a summary of the paper in § 6.

2. OBSERVATIONS AND DATA REDUCTION

The images presented in this paper were taken with MIRAC2, the University of Arizona/SAO mid-IR camera, at the UKIRT and IRTF telescopes on Mauna Kea. MIRAC2 is an upgrade of the original MIRAC camera (Hoffmann et al. 1993), and utilizes a Rockwell HF16 128 × 128 Si:As BIB array. A continuous zoom magnification between 0.28 and 0.56, (yielding a pixel scale of 0″.5–0″.25 per pixel at the IRTF), achieved with a moving stage for the detector, and a 75 μm pixel size allow for Nyquist sampling of a diffraction-limited PSF on both telescopes. All the observations were made in a standard mid-IR observing mode, by chopping the secondary mirror (~3 Hz) and nodding the telescope (~0.1 Hz) to subtract the background emission from the sky and telescope. Since our sources are compact (FWHM ≤ 4″) relative to the size of the array (~44″ × 44″), the chop and nod throws were set to 20″ in orthogonal directions, so that the source was on the array in each of the four beams. Observing in this manner allowed us to obtain four images of the source on the array with each observation (one chop-nod cycle) and to increase the signal-to-noise ratio (S/N) in our images by a factor of 2 in the same total integration time. The bright IR standard stars α Boo, β Peg, and γ Aql were observed frequently during the nights to provide accurate flux calibration. Pixel-to-pixel variations in the array (including

offsets between the 16 channel readout amplifiers) were eliminated by using gain matrices derived from observations of blank sky at 1 and 2 airmasses.

The wavelengths of observation were selected to obtain information on the dust continuum emission as well as on feature emission, while maximizing the sensitivity of the data. The observations of IRAS 07134 + 1005 were obtained at the UKIRT on 1994 November 28 with a pixel scale of 0″.25 per pixel. The data were taken over a five hour period under excellent "seeing," and the images are near diffraction-limited. Images were taken in the 8.8, 11.7, and 20.6 μm broadband filters, the narrowband 17.4 μm filter and with the circular variable filter (CVF) at 12.8 and 13.1 μm. IRAS 22272 + 5435 was observed at the IRTF, also under good atmospheric conditions, on the night of 1995 May 30 with a scale of 0″.39 per pixel. Images were obtained at 8.8, 11.7, 12.5, 17.8, and 20.6 μm, as well as with the CVF. A summary of all of the observations is presented in Table 1.

The images were first corrected for atmospheric extinction using the median extinction values for broadband filters from the UKIRT manual (Krisciunas et al. 1987). Observations of our sources as well as the standard stars were made at low (≤1.3) airmass, and therefore the correction factors are ≤10%. Standard star flux densities (Jy) were derived using magnitudes from Cohen et al. (1995) and Cohen & Davies (1995), and the revised zero-magnitude flux densities of Cohen et al. (1992). Our fluxes for both sources are within 10%–15% of flux densities estimated from the IRAS low resolution spectra (LRS) and/or the IRAS 12 μm broadband fluxes. Individual images at each wavelength were put together using a cross–correlation routine. The cross correlation was performed separately on each of the four source images (chop pair and nod pair) on the array; four sets of images were then averaged together using the offsets derived from the cross-correlation routine. Finally, each of the four (shifted and averaged) source images were extracted, then combined using the same procedure. The final images are presented in Figures 1 and 2. In each panel, the FWHM of the standard star is shown in the lower left corner.

2.1. IRAS 07134 + 1005

The dust emission from IRAS 07134 + 1005 is well resolved in our images, shown in Figure 1. The peak

TABLE 1
SUMMARY OF MIRAC2 OBSERVATIONS

Object	λ (μm)	$\Delta\lambda/\lambda$	Noise (1 σ) (Jy arcsec^{-2})	Peak (Jy arcsec^{-2})	Flux Density[a] (Jy)
IRAS 07134 + 1005......	8.8	10%	0.02	0.9	7.8 ± 1
	11.7	10%	0.03	3.0	30 ± 3
	12.8	1.8%	0.08	3.3	33 ± 3
	13.1	1.8%	0.08	3.6	35 ± 4
	17.4	2.6%	0.11	5.0	54 ± 8
	20.6	6.8%	0.14	14.6	145 ± 15
IRAS 22272 + 5435......	8.8	10%	0.01	8.2	27 ± 3
	11.7	10%	0.02	26	102 ± 10
	12.5	10%	0.02	26	105 ± 10
	13.1	1.8%	0.07	24	98 ± 10
	17.8	2.6%	0.13	31	163 ± 20
	20.6	6.8%	0.08	40	234 ± 23

[a] The uncertainty in our 8–13 μm flux calibration is approximately ±10%, but it is somewhat larger at 17 and 20 μm, where the atmosphere is more variable.
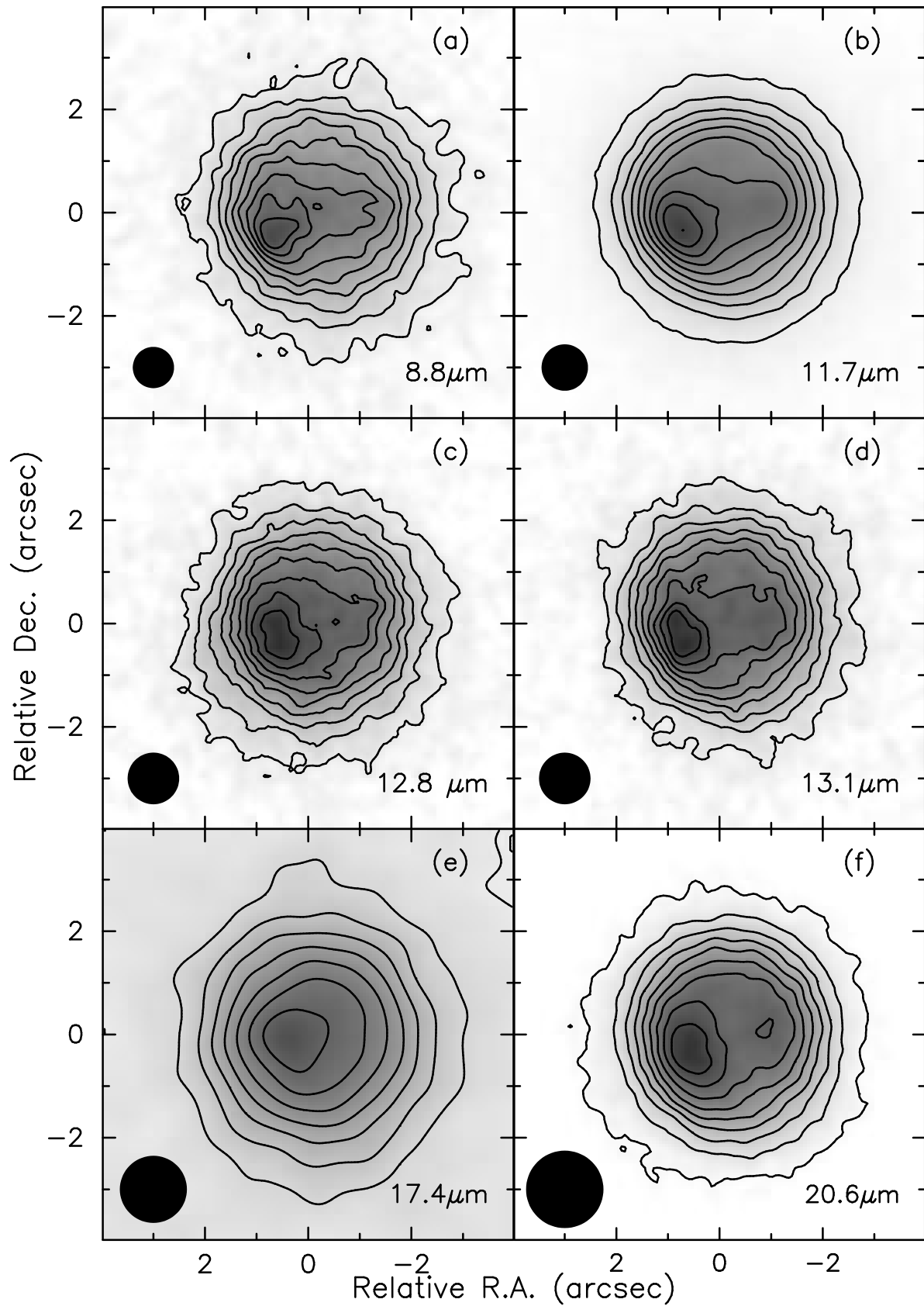
Fig. 1.—Mid-IR images of IRAS 07134 + 1005. Contour interval is 10% of the peak, given in Table 1. The FWHM of the standard star, shown at lower left, goes from 0″.7 at 8.8 μm to 1″.4 at 20.6 μm.
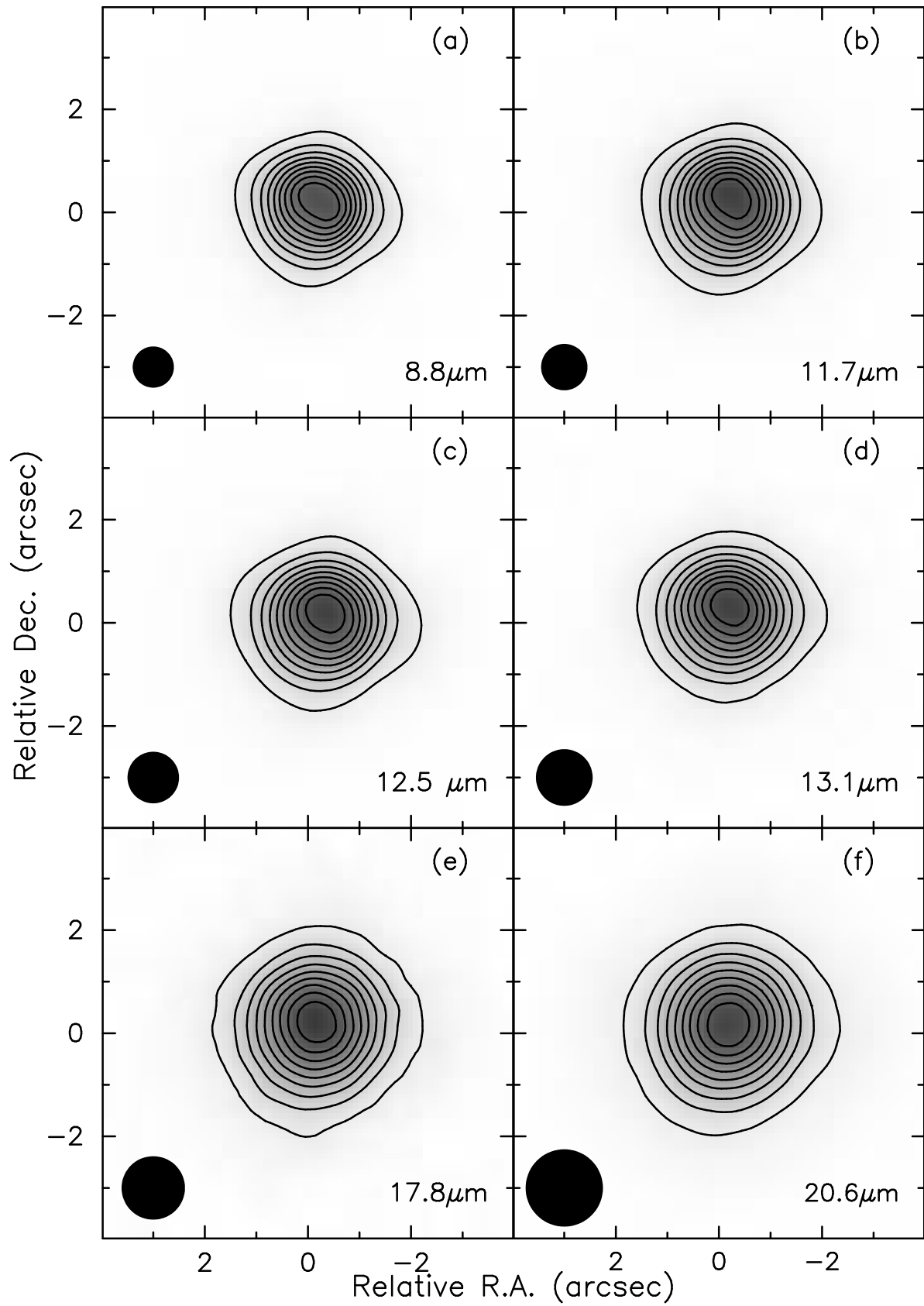
FIG. 2.—Mid-IR images of IRAS 22272 + 5435. Contour interval is 10% of the peak, given in Table 1. The FWHM of the standard star, shown at lower left, goes from 0".8 at 8.8 μm to 1".5 at 20.6 μm.

emission comes from a lobe situated about $1\rlap{.}''2$ from the nebula center along a P.A. $\approx 115°$. There is also emission from a weaker lobe diametrically opposite this bright lobe. This morphology suggests that these lobes are the limb-brightened edges of a toroidal or cylindrical shell-like dust envelope. In the plane of the sky, the axis of this dust shell lies along a P.A. $\approx 25°$. The 8.8 μm image shows a somewhat more elliptical inner region as compared to the longer wavelength images; the central part of the nebula is more filled-in, owing to a contribution from the central star. At 8.8 μm, the FWHM of the source is about $3\rlap{.}''1$ along the (north-south) symmetry axis and $3\rlap{.}''4$ in the east-west direction. The full width at zero intensity (FWZI) of the nebula along both axes is, however, about $6\rlap{.}''9$. In the 20.6 μm image, the two lobes appear to be more pronounced; the FWHM is about $3\rlap{.}''7$. At each wavelength, the eastern lobe is about 30% brighter than the western lobe. To within our resolution, we find that there is no significant difference in the spatial extent of the source at our wavelengths of observation. However, the 11.7 and 20.6 μm images have the highest S/N ratio and show faint nebulosity extending out to a radius of $\sim 4''$.

2.2. IRAS 22272 + 5435

The dust shell is centrally peaked and compact (Fig. 2), but resolved at all wavelengths. The inner contours of the shorter wavelength maps are elliptical (P.A. $\sim 50°$), but outer contours appear to show a more rectangular structure. A comparison among all of our images (convolved to the same resolution) shows no significant differences in the source extent. The source has a FWHM $\approx 1\rlap{.}''8$, but there is evidence for an extended halo of emission in the 11.7 μm image out to a radius of $8''-9''$(FWZI). The extended emission may be related to the distribution of the feature emitters, but it is also possible that the halo simply consists of faint continuum emission from cooler dust.

3. ANALYSIS AND RESULTS

From our images of thermal dust emission, we derive temperature and optical depth maps in § 3.1. In § 3.2, we derive continuum maps at wavelengths of feature emission and subtract these from observations to obtain emission feature maps. All the images used to derive temperature, optical depth, and feature maps are first registered and then convolved to the same resolution (that with the largest PSF). All calculations are then made only for regions of the images where the S/N ≥ 10.

3.1. Temperature and Optical Depth

From the solution to the equation of radiative transfer for an isothermal (along the line of sight), homogeneous nebula, the observed intensity I_ν is related to the temperature of the dust (T), optical depth of warm dust (τ_{warm}), and optical depth of cooler, foreground dust (τ_{cold}) by the equation

$$I_\nu = (1 - e^{-\tau_{\text{warm}}})B_\nu(T)e^{-\tau_{\text{cold}}} . \qquad (1)$$

If the emission is optically thin ($\tau_{\text{warm}} \ll 1$), and there is negligible extinction by cooler dust ($\tau_{\text{cold}} \approx 0$), then $I_\nu \approx \tau_{\text{warm}} B_\nu(T)$. Since absorption by dust grains is the dominant mechanism for extinction of starlight in the mid-IR region, $\tau \propto Q$, Q being the absorption efficiency. Any two measure-

ments of the intensity at continuum wavelengths allow us to calculate a physical temperature for the grains, under certain assumptions about the grain emissivity. From our images that sample dust continuum emission, we derive a temperature map for both our sources using

$$T \approx \frac{1.44 \times 10^4(\lambda_2^{-1} - \lambda_1^{-1})}{\ln\left[(I_{\nu 1}/I_{\nu 2})(\lambda_1/\lambda_2)^{n+3}\right]} \text{ K} . \qquad (2)$$

Here, we assume that the absorption efficiency (or emissivity) $Q \sim \lambda^{-n}$ and $kT \ll h\nu$. $I_{\nu 1}$ and $I_{\nu 2}$ are the observed continuum intensities at λ_1 and λ_2 (microns) in Jy arcsec^{-2}. For our derivation, we assume that $n = 0.7$, a value consistent with the calculated absorption coefficient for spherical graphite particles in this region of the spectrum (Draine & Lee 1984). For $n = 0$, we obtain temperatures that are about 20 K higher, and for $n = 2$ the temperatures are about 20 K lower. Note that if the optical depth of cooler dust surrounding the warm dust shells is significant, and follows a similar emissivity law (λ^{-n}), our calculated temperatures will be somewhat lower than the actual temperature; nevertheless, the maps will still accurately represent the relative locations of hotter and cooler grains in the nebula.

By using the Planck function and the temperature derived from equation (2), and by rearranging equation (1), we can calculate the optical depth (τ_{warm}) at λ_3 from

$$\tau_{\lambda_3} = -\ln\left[1 - \frac{I_{\nu 3}}{B_\nu(T)}\right], \qquad (3)$$

where $I_{\nu 3}$ is the observed intensity (Jy arcsec^{-2}) at λ_3. Once again, this calculation assumes negligible extinction by cold dust along the line of sight to the nebula.

Figure 3 shows the temperature and optical depth maps for IRAS 07134 + 1005. Because of the plethora of emission features, it is difficult to obtain broadband images that do not mix feature emission with the continuum emission. For IRAS 07134, we derive the temperature map from our 8.8 and 17.4 μm images. The 8.8 μm filter probably contains some feature emission from the 6–9 μm plateau in addition to the dust continuum. However, this broad feature centered near 8 μm drops sharply between 8.4 and 8.8 μm (Justtanont et al. 1996; Buss et al. 1990); hence, these 8.8 μm images largely represent continuum emission from the warm dust. The temperature shown in Figure 3a is quite uniform over the dust shell; it varies from 160 to 190 K, with an average of about 180 K. The calculated noise in the temperature map is ≈ 5 K, based on the noise in the continuum images and its propagation through the above calculations. The optical depth maps of IRAS 07134 at various wavelengths indicate that the nebula is optically thin and that the observed bipolar lobes are regions of highest column density. The optical depth maps look similar at all wavelengths; the optical depth map at 20.6 μm is shown in Figure 3b. The peak optical depth at 20.6 μm, $\tau_{20.6} \sim 0.006$, occurs in the southeast lobe of the nebula.

The temperature map for IRAS 22272, shown in Figure 4a, is derived from the 8.8 and 17.8 μm observations. The temperature appears to vary from about 190 K toward the center of the nebula to about 165 K near the edges. The isotherms are elliptical along a P.A. $\sim 55°$. The eccentricity suggests that the warmer dust emission could be confined to a disk tilted 30°–40° (from face-on) along the line of sight. The 20.6 μm optical depth map of IRAS 22272 is shown in
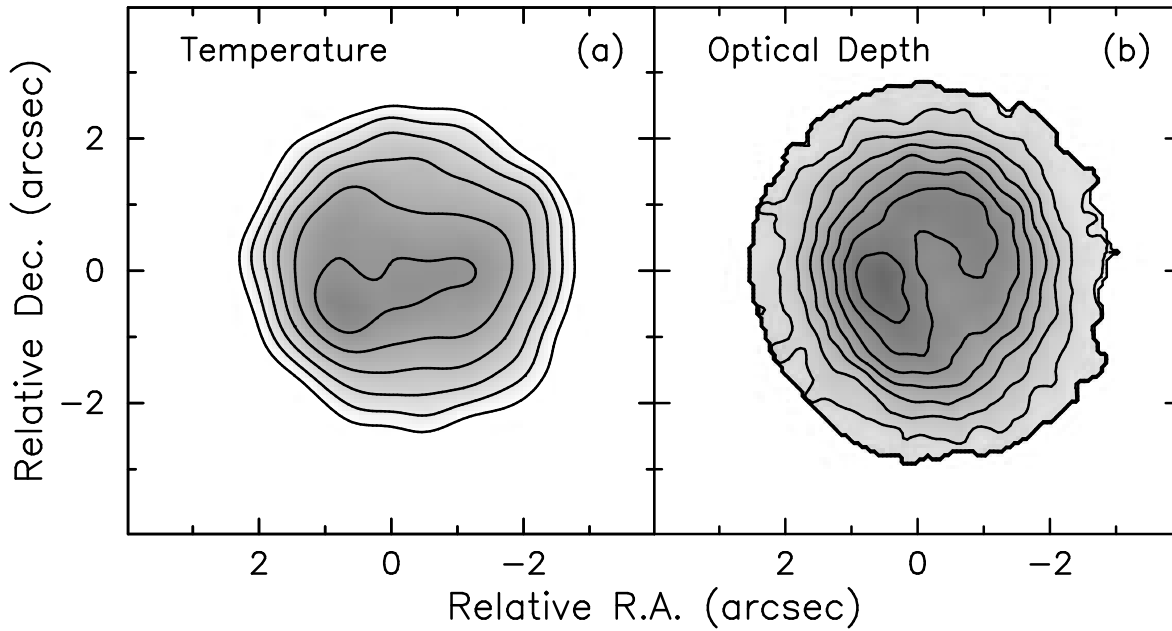
FIG. 3.—Temperature and optical depth maps of IRAS 07134+1005. (a) Temperature map derived from the 8.8 and 17.4 μm images; contours go from 160 K to 185 K in steps of 5 K. (b) Optical depth map at 20.6 μm; contour interval is 10% of the peak optical depth, which is 0.006.

Figure 4b. The peak optical depth, $\tau_{20.6} \sim 0.016$, occurs toward the center of the nebula. The contours show a somewhat elliptical distribution, with a P.A. $\approx -30°$. The direction of the major axis is almost perpendicular to the axis of the isotherms; however, the deviation from spherical symmetry is uncertain, given the resolution of our data and the compactness of the source.

Our optical depth maps for both sources clearly show that the mid-IR emission is optically thin, and that we are justified in modeling the morphology of these sources using simple, optically thin models.

3.2. Feature Emission

The mid-IR spectra of both IRAS 07134 and IRAS 22272 show two strong spectral emission features at 11 and 21 μm; one of the questions we attempt to answer from our data is whether there are any spatial variations in the feature to continuum emission, and if so, whether these variations are related to the temperature and/or optical depth maps. We use our temperature maps and continuum images to construct maps of the expected continuum emission at 11.7 and 20.6 μm. We then subtract the continuum maps from the
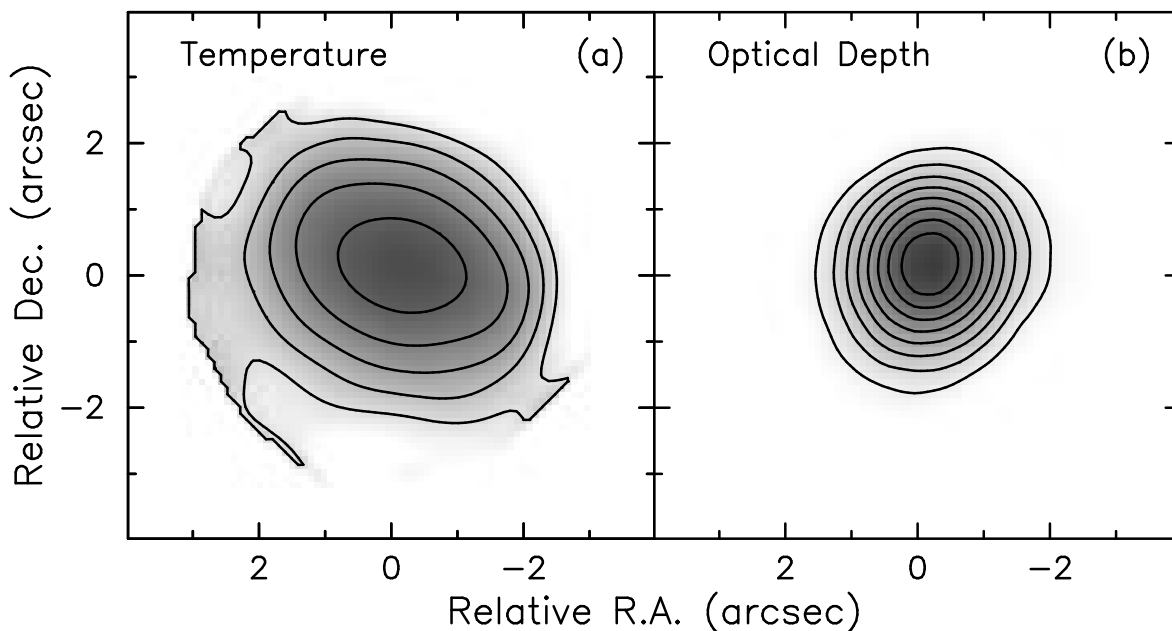

FIG. 4.—Temperature and optical depth maps of IRAS 22272+5435. (a) Temperature map derived from the 8.8 and 17.8 μm images; contours go from 165 K to 185 K in steps of 5 K. (b) Optical depth map at 20.6 μm; contour interval is 10% of the peak optical depth, which is 0.016.

observed maps and divide by the continuum maps, to obtain maps of the feature-to-continuum ratio, R. R can then be used to *estimate* the abundances of the feature carriers.

The IRAS 07134 11.7 μm ratio map (Fig. 5a) shows that R varies from 0.1 to 0.7 over the nebula, with an average value of 0.5 in the central region (defined by a 2″ radius). Although the ratio is fairly constant toward the central regions of the nebula, it shows two modest peaks that appear to coincide with the bipolar lobes of the nebula. Integration over the source indicates that the feature emission contributes about 35% of the total flux at 11.7 μm. At 20.6 μm, the feature emission is extremely strong. The 20.6 μm feature-to-continuum ratio map (Fig. 5b) shows that R ranges from 1.9 near the nebula center to 2.8 in the bright southeast lobe and 2.4 in the weaker northwest lobe, with an average value of ≈ 1.9. By integrating over the source, we calculate that the feature emitters contribute about 65% of the total flux in our filter. Our results indicate that the feature-to-continuum ratio peaks in the bipolar lobes, the regions of highest dust density. There appears to be a central cavity (surrounding the central star) where there is a deficiency of dust grains, and where the feature-to-continuum ratio is lower.

A similar analysis of IRAS 22272 shows that the 11.7 μm feature-to-continuum ratio, shown in Figure 6a, varies from 0.25 to 0.5, with an average value of 0.4. The ratio peaks at about 2″ southeast of the center of the nebula. Comparing the 11.7 μm feature map (Fig. 6a) to the temperature map (Fig. 4a), it appears as though these emitters are displaced, somewhat asymmetrically, about the major axis of the isotherms. The 21 μm feature emission, shown in Figure 6b, is much weaker than the 11.7 μm feature, and also appears quite different in its spatial distribution. Unlike the 11.7 μm, the 21 μm feature-to-continuum ratio peaks toward the center of the nebula and drops off sharply with distance away from the center. The increase in R along the periphery of the feature map may be an artifact of the image-analysis

procedure. R varies from 0.01 to 0.5, with an average value of 0.25 in the central (radius 3″) region of the nebula. Integrating the feature emission over the nebula, we find that the 11.7 μm feature contributes 30% to the total observed emission. The weaker 21 μm emission feature contributes about 20% of the total emission in our 20.6 μm images. The spatially averaged feature-to-continuum ratios derived above generally appear to agree with the spectra of Buss et al. (1990) and Justtanont et al. (1996).

The average feature-to-continuum ratios derived above provide a measure of the fraction of the total flux emitted by the carriers of a feature relative to that emitted by the dust continuum emitters, averaged over our filter bandpass. These ratios can be converted into a ratio of the total stellar flux *absorbed* by the mid-IR feature carriers relative to the continuum by including a correction factor γ such that γR is the ratio of the integrated flux in the UIR band to that in the mid- and far-IR continuum. Buss et al. (1990) show that in IRAS 22272, the 12 μm feature contains about 10% of the total far-IR flux; here, $\gamma R \approx 0.1$, or $\gamma \sim 0.1$–0.2 for R in the range 0.5–1.0. We stress that the main goal of the following abundance calculations is to illustrate how abundances of the UIR feature carriers may vary spatially over the nebulae. The absolute abundances, though important, can only be calculated accurately after the carriers have been identified and their optical properties well understood. Assuming that the feature emitters are PAH molecules, it is possible to estimate the abundances of the carriers (per H atom) from the dust and PAH opacities (Allamandola et al. 1989). The dust opacity is proportional to the observed UV/visual extinction. From the interstellar extinction curve and the optical total-to-selective extinction ratio (Spitzer 1978; Savage & Mathis 1979), we can derive the total visual extinction cross section per H atom, $A_v/N_H \approx 5 \times 10^{-22}$ cm^2. This can then be converted to a dust UV opacity, κ_{dust}, by scaling by the ratio of UV and visual dust opacities. The UV absorption cross section of PAH molecules, measured per C atom, is taken to be 7×10^{-18} cm^2 C^{-1} (Joblin et al.
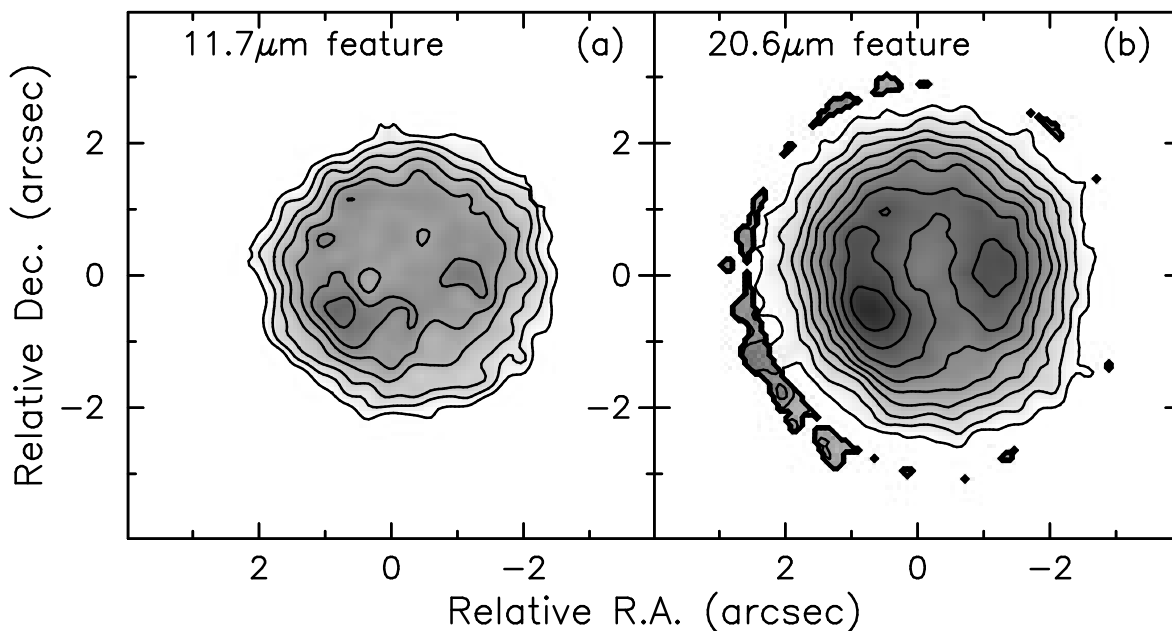

Fig. 5.—IRAS 07134 + 1005 feature-to-continuum ratio maps. (a) 11.7 μm ratio; contour levels go from 0.1 to 0.7, with an interval of 0.1. (b) 20.6 μm ratio; contour levels go from 0.2 to 2.9, with an interval of 0.3. The nonzero regions around the main disk are artifacts produced by ratioing images.
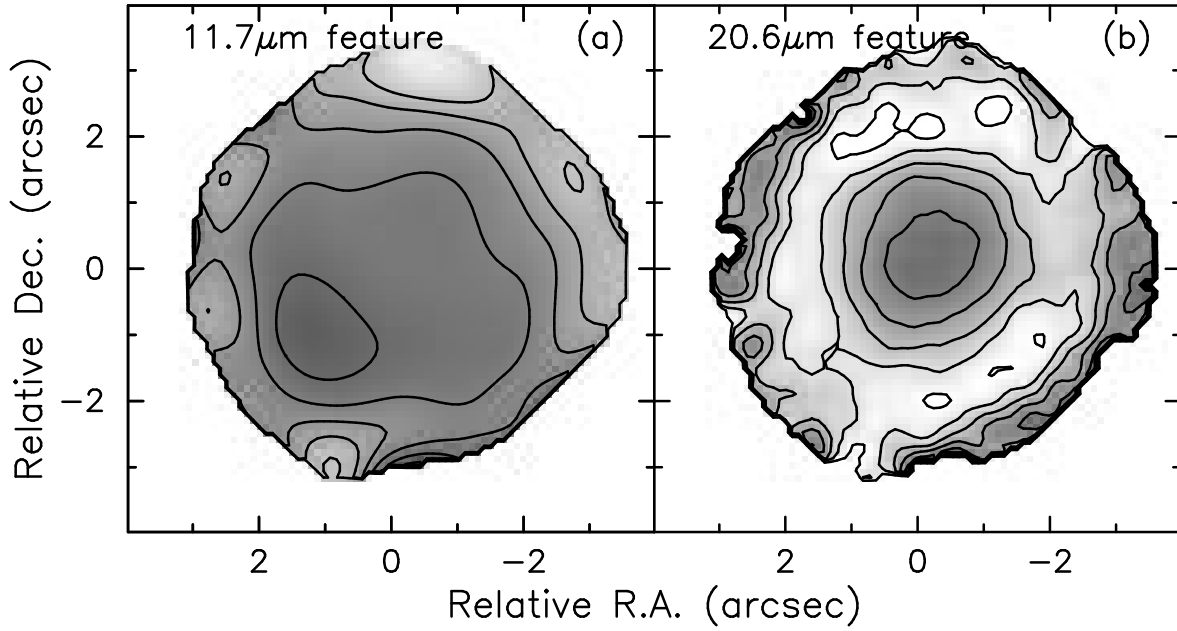
FIG. 6.—IRAS 22272+5435 feature-to-continuum ratio maps. (a) 11.7 μm ratio; contour levels go from 0.25 to 0.5, with an interval of 0.05. (b) 20.6 μm ratio; contour levels go from 0.1 to 0.6, with an interval of 0.1.

1992, Allamandola et al. 1989). Based on their study of the 3.3–11.3 μm emission bands, Allamandola et al. (1989) found that the fraction of energy emitted by the emission features is relatively insensitive to the spectral type of the illuminating stars; this suggests that the absorption cross section of the carriers of the feature emission (κ_{pah}) has a wavelength dependence similar to that of the continuum emitters. It is important to keep in mind that the study of Allamandola et al. (1989) was based on a small sample of sources with considerably higher excitation central stars than the sources presented here. For our sources, where the central stars radiate most of their energy at visible wavelengths, we simply assume that the ratio of dust to PAH opacity is well approximated by the UV opacity ratio and that the dust continuum cross section is $\kappa_{dust} = 10^{-21}$ cm² per H atom. γR is then related to the PAH and dust opacities by

$$\gamma R \approx \frac{\kappa_{pah} N_{pah} \delta}{\kappa_{dust} N_{H}}, \qquad (4)$$

where N_{pah} and N_H are the total number of PAH molecules and H atoms, respectively, and δ is the number of carbon atoms per PAH molecule. The abundance of PAHs is then given by

$$\frac{N_{pah}}{N_H} \approx \frac{1.4 \times 10^{-4} \gamma R}{\delta}. \qquad (5)$$

Applying this equation to our feature maps, using the average feature-to-continuum ratio R and assuming a PAH size of 100 carbon atoms for all the feature carriers (i.e., $\delta = 100$), we find that the 11 μm carriers have an abundance of 7×10^{-7} γ in IRAS 07134 and $5.6 \times 10^{-7} \gamma$ in IRAS 22272. For the same PAH size of 100 C atoms per PAH, the 21 μm feature carriers have an abundance of $2.7 \times 10^{-6} \gamma$ in IRAS 07134 and $3.5 \times 10^{-7} \gamma$ in IRAS 22272. For $\gamma = 0.2$,

we calculate PAH abundances of $\sim 5 \times 10^{-8}$ to 5×10^{-7}. Since these calculations assume a fixed PAH size of 100 C atoms, the abundance of the amount of carbon locked up in PAHs (with respect to H) is then $\sim 5 \times 10^{-6}$ to 5×10^{-5}. Our images show that the feature-to-continuum ratio varies significantly over the nebulae. The maps suggest that the feature carriers are more easily destroyed in regions where the dust optical depths are lower, i.e., where there is less shielding from the central star.

4. MODELING OF SOURCE MORPHOLOGY

4.1. Model Description

The images of both of our sources are inconsistent with the simplest expected morphological structure of a PN or PPN as a spherical, uniformly expanding dust shell surrounding the central star. The images of IRAS 07134 clearly show resolved bipolar lobes of emission. The images of IRAS 22272 show that at 8.8 and 11.7 μm the inner core is elliptical; at the same time, the outer contours are somewhat rectangular and show definite deviations from circular symmetry. Furthermore, the temperature map has an elliptical shape that suggests that the warmest dust lies in a disk tilted to our line of sight (see § 3.1). The morphologies of both objects suggest that the dust distribution resembles a cylindrical or toroidal shell surrounding the central star; the increased equatorial emission may represent a higher equatorial temperature and/or dust density. With these observations as motivation, we have constructed geometrically simple, optically thin models that fit the observed mid-IR morphology, as well as the mid- and far-IR flux densities of the observed PPN. Since the 11–13 μm and 21 μm data points are dominated by feature emission, we have fitted the continuum level at these wavelengths as calculated in § 3.2.

For our models, we assume that the central star is surrounded by two dust components: a warm dust component

represented by a cylindrical shell, which is responsible for most of the observed mid-IR emission, and a cooler, more extended spherical dust shell that produces most of the far-IR luminosity. A schematic of the model geometry is shown in Figure 7. The cylindrical shell is the simplest axisymmetrical shape that can represent a period of enhanced mass loss in the equatorial plane. The cooler spherical shell represents dust that extends farther out from the central star, possibly driven out before the development of asymmetry in the mass-loss process. Since the equilibrium temperature of dust grains in a nebula depends on their rates of heating and cooling, the two temperature components may also be interpreted as two distinct grain populations, differing in their average size and/or emissive properties. Under the assumption that the emission is optically thin, the model surface brightness is simply derived by integrating the emission at each point on the projected surface of the nebula along the line of sight. The model images are then convolved to the same resolution as the observations and compared directly with our 10 and 20 μm images. The inclination of the cylindrical shell toward the observer (θ) determines the ellipticity of the nebula; limb brightening along lines of sight through the walls of the cylinder create the observed bipolar emission lobes. The inner and outer radii (R_{in} and R_{out}) of the cylinder determine the width and separation of the lobes. Although the model images allow us to determine the geometry of the sources, the SED (derived by integrating fluxes over the images at multiple wavelengths) is more useful as a diagnostic for constraining the temperatures and masses of the dust shells. We derive model flux densities at wavelengths for which we have measurements to compare with the model predictions. The 8–20 μm model fluxes are compared with our data; the 60 and 100 μm fluxes are constrained by the IRAS broadband measurements. For IRAS 22272, measurements of thermal emission at 1.3 mm (Walmsley et al. 1991) are used as an added constraint on the model parameters. It is especially important to include the far-IR ($\lambda > 25$ μm) fluxes in constraining our model. The far-IR emission characterizes a cooler ($T_d \approx 80$ K) dust population that is not a significant contributor to the mid-IR emission, but contains a large proportion of the total dust mass. Therefore, any models of the total dust mass based only on mid-IR observations are likely to severely underestimate the total mass of the nebulae.

We find that the mid-IR fluxes for both sources can be fitted quite well by a single Planck function. This suggests that there is no significant contribution to the integrated dust continuum emission from the central star, even at 8.8 μm. However, since the emission from the star is concentrated toward the center of the nebula, it is entirely possible that its emission may be a small, but noticeable, fraction of the flux in the central few pixels of our images. The effect of the central star should therefore be much stronger in the well-resolved images of IRAS 07134 + 1005 than in those of IRAS 22272 + 5435. We have run models for our two sources both with and without the central star, and we find that the presence of the central star improves the model images of IRAS 07134 + 1005 quite significantly, but has a very small effect on those of IRAS 22272 + 5435.

4.2. Model Parameters

1. *Size.* The geometry of the cylindrical shell is well constrained by our 10–20 μm images. The size (inner and outer radii, height) and tilt of the shell determine the position and size of the lobes and the ellipticity of the source. For IRAS 22272 + 5435, the inner radius of the shell is unresolved; hence, we simply assume that the size (diameter) of the cavity is half the FWHM of the standard star image at 8.8 μm, i.e., $R_{in} \approx 0\overset{''}{.}2$. As there is no spatial information from the IRAS measurements at 60 and 100 μm, the outer radius of the cooler, spherical shell is not well constrained; however, we find that changing the outer radius weakly affects the emission (radial profiles) in the inner regions of our 17–20 μm model images (for a given total mass and density power law).

2. *Temperature.* The observed 10–20 μm MIRAC2 images, together with the IRAS 60 and 100 μm fluxes, rule out an isothermal, single-temperature model. We determine the temperature of the warmer component from our calculated temperature maps. The temperature and fraction of the cooler dust is then derived by iteratively fitting the SED from 8–100 μm. The temperatures of the two dust components are well constrained, and can be derived independently of the geometrical parameters.

3. *Density.* The density is assumed to follow a power law, $\rho \sim R^{-\alpha}$. An R^{-2} density law, consistent with a constant mass-loss rate and expansion velocity in an expanding spherical envelope, produces images that are too sharply peaked at the center. However, a power law with $\alpha \approx 1$ gives a reasonable fit to both images. This value of α is consistent with a scenario in which the expansion velocity, V_{exp}, is proportional to R^{-1} (i.e., higher velocities closer in to the central star), or a scenario in which the mass-loss rate has decreased with time.

4. *Grains.* We assume that the dust is composed of spherical graphite grains of radius 0.1 μm and that the emissivity of the grains is $Q_\lambda \sim \lambda^{-0.7}$. This grain size agrees with measurements of grain sizes in IRC + 10216 and AFGL 2688 (as well as a number of oxygen-rich AGB stars), but is smaller than grains in AFGL 915 (Jura, Balm, & Kahane 1995; Jura 1996; Jura, Turner, & Balm 1997). The exponent is consistent with calculations of Draine & Lee (1984) over the 10–100 μm range. To fit the measured flux density of IRAS 22272 + 5435 at 1.3 mm, we varied n (for $\lambda \geq 100$ μm)
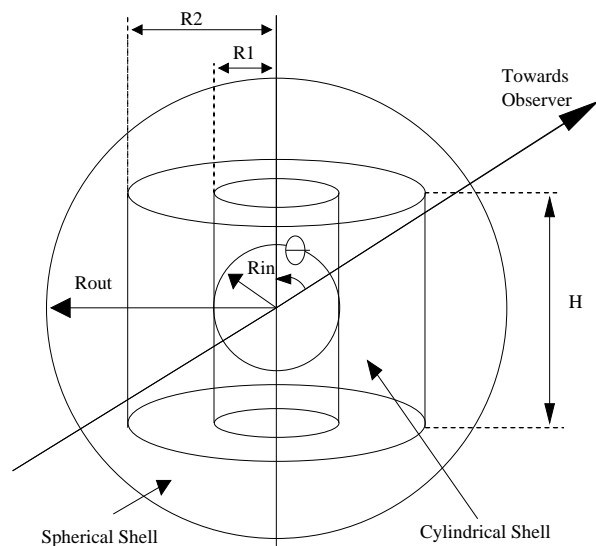

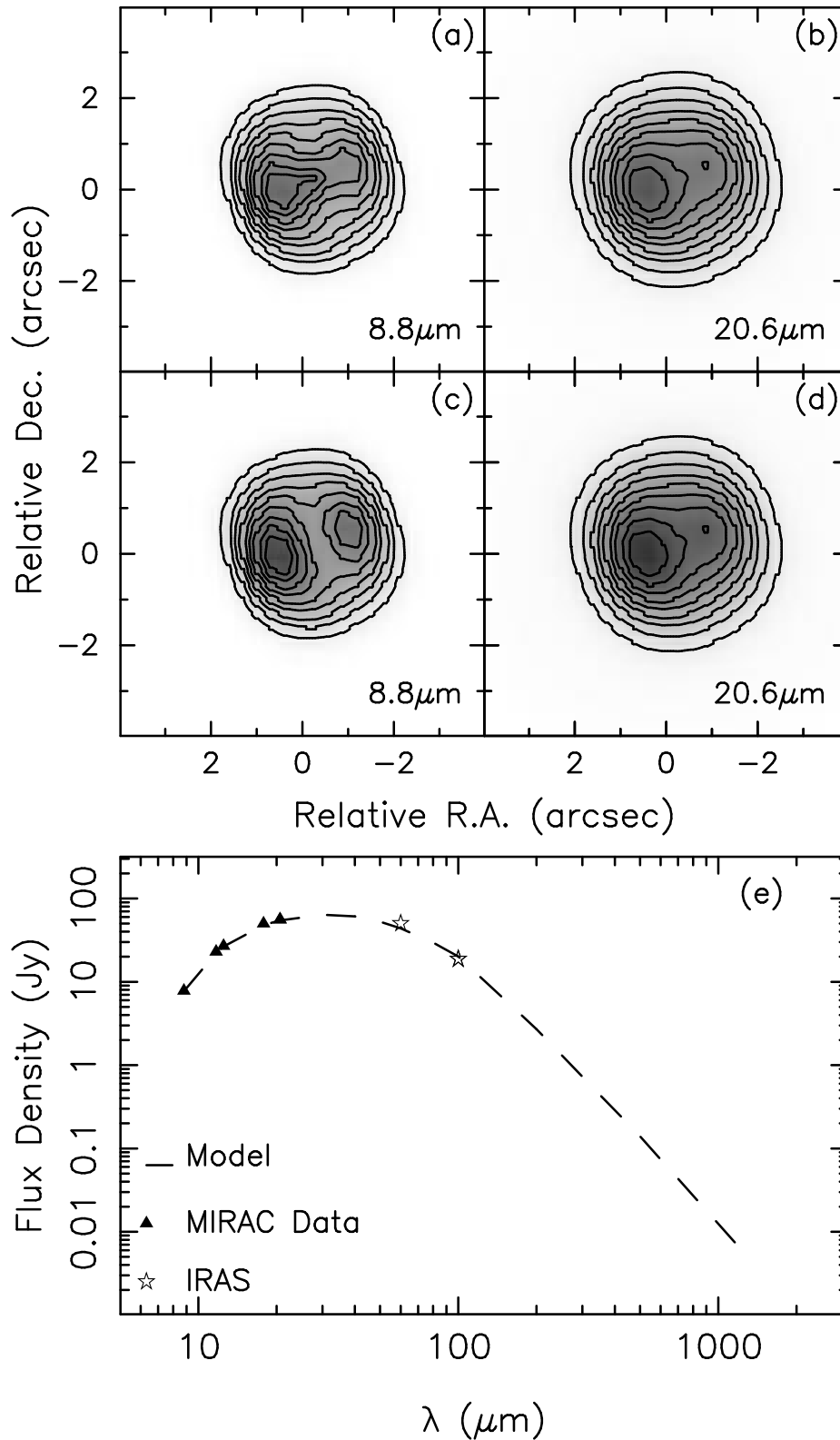FIG. 7.—Schematic of model geometry. See text for model description.

Fig. 8.—IRAS 07134 + 1005 8.8 μm and 20.6 μm model images and SED. (*a*)–(*b*) Model images with contribution from a $10^4 L_\odot$ central star. (*c*)–(*d*) Model images without central star. (*e*) Model SED and data. Compare with Figs. 1*a* and 1*f*.

between 1 and 2, and found that $n = 1.5$ gave the best fit to the data. From the images of IRAS 07134 + 1005, it is clear that the southeast lobe is brighter than the northwest lobe. We find that to fit this anomaly with our optically thin

models, we need a 30% density enhancement in the eastern half of the nebula.

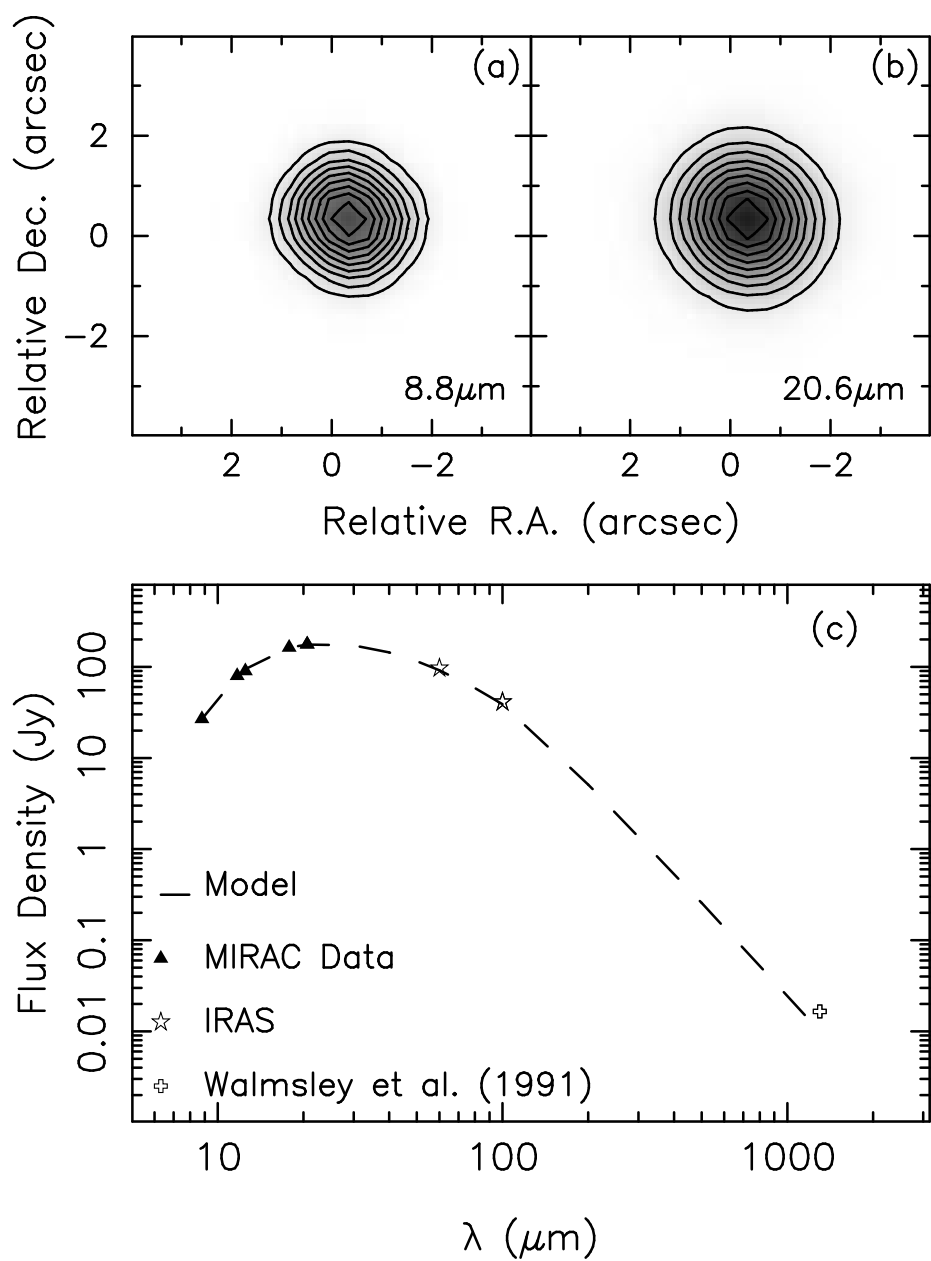5. *Central Star*. Optical spectroscopy of IRAS 22272 + 5435 and IRAS 07134 + 1005 (Hrivnak 1995;

FIG. 9.—(a)–(b) IRAS 22272 + 5435 8.8 μm and 20.6 μm model images. (c) Model SED and data. Compare with Figs. 2a and 2f.

Hrivnak et al., 1989) reveals that the central stars are classified as G5 and F0–5 supergiants respectively. For our models, we assume that the central star of IRAS 22272 + 5435 has a temperature of 5200 K, and that of IRAS 07134 + 1005 a temperature of 6800 K. We find that our best-fit model for IRAS 07134 + 1005, which includes a contribution from the central star at 8.8 μm, indicates an effective (optical) radius of $\sim 86\ R_{\odot}$, and constrains $L/$

TABLE 2

SUMMARY OF MODEL PARAMETERS

	CYLINDER					SPHERE					
OBJECT	$R1^{a}$ (cm)	$R2^{a}$ (cm)	H^{a} (cm)	T_1 (K)	θ (deg)	$R_{in}{}^{a}$ (cm)	$R_{out}{}^{a}$ (cm)	T_2 (K)	f_c	d^{b} (kpc)	$M_{total}{}^{c}$ ($M_{\odot}$)
IRAS 07134......	1.2	2.7	5.4	190	40	1.2	9.0	80	0.92	2.7	0.26
IRAS 22272......	0.3	1.8	2.8	190	65	0.3	9.8	80	0.80	2.7	0.42

[a] Divided by 10^{16}.
[b] See text for discussion.
[c] Assumes $M_{gas}/M_{dust} = 200$

$d^2 \sim 1.5 \times 10^3 \; L_\odot \text{kpc}^{-2}$. For IRAS 22272+5435, we believe that the emission from the dust shell completely dominates over emission from the central star for $\lambda \geq 8.8$ μm. Therefore, we obtain no constraints on the parameters of the central star.

6. *Distance*. We adopt a value of 2.7 kpc for the distance to IRAS 22272+5435. This is based on the galactic rotation model calculation by Woodsworth, Kwok, & Chan (1990), who observed CO toward this object. For IRAS 07134+1005, there is no reliable distance measurement. From our image constraints on L/d^2 (see above paragraph) and assuming $L_* \sim 10^4 \; L_\odot$, we estimate the distance to IRAS 07134+1005 to be about 2.5–3 kpc; for our models, we simply use a value of 2.7 kpc for this source as well.

4.3. Model Results

Our models allow us to constrain the geometry of the warm dust shell, the total mass of dust in the nebulae, and the temperature and fraction of warm and cool dust grains, and to set dynamical constraints on the mass-loss rate (from the density law). Our assumptions about two fixed grain temperatures are obviously simplifications of the physical structure of these nebulae. Since the central star is the dominant heating source in these objects, there is likely a temperature gradient through the dust shells. However, from our maps of the dust temperature, we find that there is a relatively small ($\leq 20\%$) change in the temperature over the face of the nebulae (see § 3.1). Furthermore, we have explored models that include a temperature gradient; we find that these models are ineffective in constraining our fits any better—they simply add more free parameters. Our best-fit model images and SEDs are presented in Figures 8 and 9. The model images of IRAS 07134 (Figs. 8a and 8b) can be directly compared with the observed 8.8 and 20.6 μm images shown in Figures 1a and 1f. Clearly, there is good agreement between the data and the model. In particular, the model reproduces the elongated inner contours observed in the 8.8 μm image as well as the more spherical inner contours of the 20.6 μm image. The model also matches the overall shape and extent of the nebula. Figures 8c and 8d illustrate the effect of removing the contribution of the central star from the best-fit model. Although this has little or no effect on the 20.6 μm model image, the 8.8 μm model image without the central star (Fig. 8c) differs significantly from the observed 8.8 μm image (Fig. 1a); the model nebula appears less "filled-in" toward the center, and now has more pronounced bipolar lobes than the data. There is an obvious asymmetry in the two emission lobes toward IRAS 07134, which we model simply by assuming a density enhancement (by 30%) in one half of the nebula. Although our optically thin axial models do not explain this asymmetry, we suggest that a slightly modified geometrical model, in which there is absorption of mid-IR emission by cooler dust in the outer regions of the cylindrical or toroidal shell, could produce lobes of unequal brightness. The actual mechanism may be similar to that proposed by Hora et al. (1996) to account for variations in the intensity of the optical lobes of AFGL 2688. In AFGL 2688, because of the tilt of the nebula, one lobe is seen through a significantly larger amount of cooler dust in the equatorial plane. The model SED shown in Figure 8e also fits the observed fluxes quite well and allows us to determine the temperature and the relative proportions of the two components. Figures 9a and 9b show the best-fit model images of IRAS 22272 and

are to be compared with the images in Figures 2a and 2f. Here too, the images reproduce the general morphology of the source, including the overall rectangular (or quadrupolar) structure, but since this source is more compact, the geometrical parameters are less well determined. The SED fit is, however, well determined; the temperature, proportion, and emissivity of the cooler grains is more tightly constrained by the IRAS 60 and 100 μm fluxes and the 1.3 mm bolometer flux measurement by Walmsley et al. (1991).

As stated in § 4.2, we determine the temperature of the two components and their relative proportions iteratively, by fitting the observed SED. For both sources, the warmer dust temperature is $T_1 \approx 190$ K. For IRAS 07134+1005, the cooler dust lies between 80–100 K and the corresponding cool dust fraction is $f_c \approx 94\%$–90%. In the case of IRAS 22272+5435, a wider range of cooler dust temperatures provides satisfactory fits to the SED: $T_2 \approx 60$–90 K, corresponding to a range in the mass fraction of $f_c \approx 94\%$–80%. In each case, a significant proportion of the total dust mass is in the form of cool (≈ 80 K) grains, but IRAS 07134+1005 appears to have a larger fraction of mass in cooler grains. For IRAS 22272, we derive a total dust mass of $M_d \sim 2.1 \times 10^{-3} \; M_\odot$. Assuming a gas-to-dust ratio of 200, this yields a total nebular mass of $\sim 0.42 \; M_\odot$. For IRAS 07134+1005, we derive a dust mass of 1.3×10^{-3} $M_\odot$ and a total nebular mass of $0.26 \; M_\odot$. The parameters of our best-fit models are summarized in Table 2.

5. DISCUSSION

5.1. Morphology

One of the most successful theories proposed to explain the shaping of PNs has been the interacting stellar winds (ISW) model (e.g., Icke, Balick, & Frank 1992; Soker & Livio 1989; Kahn & West 1985; Kwok, Purton, & Fitzgerald 1978). The ISW model can account for the variety of observed PN morphologies (Corradi & Schwarz 1995; Balick 1987; Zuckerman & Aller 1986) if there is a large equator-to-pole density contrast in the slow AGB wind. (This density contrast is what gives PPNs an elliptical or toroidal appearance.) Hydrodynamical calculations show that even small asymmetries in the slow AGB wind can result in pronounced axisymmetric structures as the fast PN wind interacts with it. However, although the ISW models can explain most PN morphologies (especially when orientation of the nebula is also taken into account), they do not explain the origin of the density contrast in the AGB wind. A detailed discussion of the various mechanisms that have been invoked for this density contrast are beyond the scope of this paper; these include binary interactions and stellar rotation (e.g., Dorfi & Höfner 1996; Livio 1994; Bond & Livio 1990) and magnetic fields (Chevalier 1994). Optically thin cylindrical and/or ellipsoidal models are merely simpler representations of an equator-to-pole density contrast. Our models suggest that the mid-IR morphologies of IRAS 07134 and IRAS 22272 indicate a fairly high equator-to-pole density contrast, and are at least qualitatively consistent with the results of Meixner et al. (1997), who find $\dot{M}_{\text{equator}}/\dot{M}_{\text{pole}} \approx 18$. Models similar to ours have been constructed previously for a variety of PNs (Hora et al. 1990; Masson 1990; Balick, Preston, & Icke 1987; Bentley et al. 1984). These models showed that even relatively simple axially symmetric structures could simulate the morphol-

ogies of some PNs. From observations of the dust emission, it has now become quite clear that axial symmetry in the dust envelope develops during, or soon after a star leaves, the AGB and is well established by the time the source becomes a PPN.

5.2. Carrier Abundances

A variety of candidates have been proposed to account for the unidentified 21 μm feature (Justtanont et al. 1996; Montou, Léger, & d'Hendecourt 1996; Goebel 1993; Sourisseau, Coddens, & Papoular 1992). Since this feature appears to be associated with carbon-rich PPNs, which also show strong emission features in the 3–13 μm range, it seems likely that the carriers of all of these features are closely related. Furthermore, the fact that the 21 μm feature is not seen in evolutionary stages preceding or following those of these few PPNs suggests that the carriers are rather fragile. Buss et al. (1990) showed that the strengths of the 12 and 21 μm emission bands in IRAS 22272 and IRAS 07134 cannot be explained by UV pumping alone. Unlike the conventional PAH molecules, which have a low optical/UV absorption cross-section ratio (Allamandola et al. 1989), these carriers are excited primarily by visible photons. Therefore, the grains in these sources are probably larger than the typical PAH molecules and/or comprise clusters of PAH molecules. Justtanont et al. (1996) find that the 7–13 μm features can be reproduced by the simple PAH molecule chrysene ($C_{18}H_{12}$); however, chrysene does not account for the 21 μm feature. They speculate that the 21 μm feature might be attributed to superhydrogenated PAH molecules (SPAHs; Schutte, Tielens, & Allamandola 1993), which become dehydrogenated and ionized as the central star gets hotter. Montou et al. (1996) have investigated the absorption spectra of PAHs in the 14–75 μm range; their results show that large PAHs (> 500 atoms) have emission bands at 16.2, 18.2, 21.3, and 23.1 μm. Although not all of these bands have been seen in the spectra of interstellar sources, Montou et al. (1996) suggest that families of such PAHs may be responsible for the broad 21 μm emission feature; however, any model claiming that these PAHs are responsible for the 21 μm feature must also explain the absence of the 16–18 μm features in the 21 μm sources. Beintema et al. (1996) have recently observed three PNs with the Short Wavelength Spectrometer (SWS) aboard *ISO* and report the detection of an emission feature near 17 μm; this feature has not been seen in previous ground-based spectra. They suggest that this feature, *if real*, may be closely related to the 21 μm feature. The 16–48 μm spectra of both IRAS 22272 and IRAS 07134 taken by Omont et al. (1995) with the KAO show a broad emission feature from about 25 to 40 μm, with a peak near 30 μm. In the case of IRAS 07134, the 21 μm feature appears to be significantly brighter than and distinct from the broad 30 μm feature; in contrast, the 21 μm feature in IRAS 22272 is much weaker than the 30 μm feature, and appears to merge with it. However, unlike the 21 μm feature, the 30 μm emission band has been seen in a larger number of objects, including the PN IC 418. Hence, there is no clear correlation between the two bands.

The observed spatial variations in the feature-to-continuum emission ratio at 11 and 21 μm depend not only on the abundance of the carriers, but also on their UV/visible absorption properties (and the stellar radiation field). IRAS 07134, which has a hotter central star than IRAS 22272, has a significantly higher observed 21 μm/11 μm ratio. We find that a larger fraction of the total far-IR emission of IRAS 07134 (see § 4.3) occurs at longer wavelengths, implying the presence of a larger proportion of cooler ($T \approx 80$ K) dust. Therefore, the relative strengths of the 21 and 11 μm bands may also be related to the temperature of the dust grains. However, the differences in the 11 and 21 μm relative intensities (and the spatial variations) and their relation to the physical conditions in the nebulae can be understood properly only after the carriers have been conclusively identified. The ubiquity of the UIR emission bands in astrophysical environments such as H II regions, reflection nebulae, galactic nuclei, PNs, and PPNs strongly suggests that PAH-like molecules constitute a significant fraction of the cosmic carbon. From their measurements of absorption cross sections of various PAH mixtures and abundance calculations, Joblin, Léger, & Martin (1992) estimated (assuming $C/H = 3.6 \times 10^{-4}$) that PAHs contain $\sim 18\%$ of the total interstellar carbon. We estimate (see § 3.2) that in our carbon-rich PPNs, the carbon abundance in the form of PAH molecules (averaged over each source) varies from about 5×10^{-6} to 5×10^{-5}. If the total carbon abundance in these sources is $\approx 10^{-3}$, this implies that PAHs contain about 0.5%–5% of the total carbon in these stars.

6. SUMMARY

We have obtained mid-IR images of two PPNs at wavelengths of dust continuum and feature emission; the images are spatially resolved and show that neither object is spherically symmetric. Temperature and optical depth maps indicate that the dust temperature varies from 160 K to 200 K across the nebulae and that the emission is optically thin. Our feature-to-continuum ratio maps at 11.7 and 20.6 μm show that this ratio varies significantly over the central regions of the nebulae. The feature-to-continuum ratios in IRAS 07134 appear to peak in the regions of highest dust optical depths. In IRAS 22272, we show evidence that the 12 μm feature peak is offset from the center (which is also the hottest region) of the nebula. We construct optically thin models of both sources to reproduce the observed mid-IR images and the mid- and far-IR SEDs, and find that cylindrical shells of warm ($T \approx 190$ K) dust provide good fits to our images. However, an additional component of cooler dust containing about 80% to 90% of the total dust mass is required to fit the observed SEDs. From our models, we estimate total masses of 0.26 $M_\odot$ and 0.42 $M_\odot$ for the circumstellar envelopes of IRAS 07134 + 1005 and IRAS 22272 + 5435, respectively.

REFERENCES

Allamandola, L. J., Tielens, A. G. G. M., & Barker, J. R. 1989, ApJS, 71, 733
Bakker, E. J., Waters, L. B. F. M., Lamers, H. J. G. L. M., Trams, N. R., & Van der Wolf, F. L. A. 1996, A&A, 310, 893
Balick, B. 1987, AJ, 94, 671
Balick, B., Preston, H. L., & Icke, V. 1987, AJ, 94, 1641
Beintema, D. A., et al. 1996, A&A, 315, L369
Bentley, A. F., Hackwell, J. A., Grasdalen, G. L., & Gehrz, R. D. 1984, ApJ, 278, 665
Bond, H. E., & Livio, M. 1990, ApJ, 355, 568
Buss, R. H., Jr., Cohen, M., Tielens, A. G. G. M., Werner, M. W., Bregman, J. D., Witteborn, F. C., Rank, D., & Sandford, S. A. 1990, ApJ, 365, L23
Chevalier, R. 1994, in Circumstellar Media in the Late Stages of Stellar Evolution, ed. R. Clegg, I. Stevens, & W. Meikle (Cambridge: Cambridge Univ. Press), 308
Cohen, M., & Davies, J. K. 1995, MNRAS, 715, 722
Cohen, M., Walker, R. G., Barlow, M. J., & Deacon, J. R. 1992, AJ, 104, 1650
Cohen, M., Witteborn, F. C., Walker, R. G., Bregman, J. D., & Wooden, D. H. 1995, AJ, 110, 275
Corradi, R. L. M., & Schwarz, H. E. 1995, A&A, 293, 871
Dorfi, E. A., & Höfner, S. 1996, A&A, 313, 605
Draine, B. T., & Lee, H. M. 1984, ApJ, 285, 89
Goebel, J. H. 1993, A&A, 278, 226
Guillois, O., Nenner, I., Papoular, R., & Reynaud, C. 1996, ApJ, 464, 810
Hawkins, G. W., Skinner, C. J., Meixner, M. M., Jernigan, J. G., Arens, J. F., Keto, E., & Graham, J. R. 1995, ApJ, 452, 314
Hoffmann, W. F., Fazio, G. G., Shivanandan, K., Hora, J. L., & Deutsch, L. K. 1993, Proc. SPIE, 1946, 449
Hora, J. L., Deutsch, L. K., Hoffmann, W. F., & Fazio, G. G. 1996, AJ, 112, 2064
———. 1990, ApJ, 353, 549
Hrivnak, B. J. 1995, ApJ, 438, 341
Hrivnak, B. J., Kwok, S., & Volk, K. 1989, ApJ, 346, 265

Icke, V., Balick, B., & Frank, A. 1992, A&A, 253, 224
Joblin, C., Léger, A., & Martin, P. 1992, ApJ, 393, L79
Jura, M. 1996, ApJ, 472, 806
Jura, M., Balm, S. P., & Kahane, C. 1995, ApJ, 453, 721
Jura, M., Turner, J., & Balm, S. P. 1997, ApJ, 474, 741
Justtanont, K., Barlow, M. J., Skinner, C. J., Roche, P. F., Aitken, D. K., & Smith, C. H. 1996, A&A, 309, 612
Kahn, F., & West, K. A. 1985, MNRAS, 212, 837
Krisciunas, K., et al. 1987, PASP, 99, 887
Kwok, S. 1993, AR&A, 31, 63
Kwok, S., Purton, C. R., & Fitzgerald, P. M. 1978, ApJ, 219, L125
Kwok, S., Volk, K., & Hrivnak, B. J. 1989, ApJ, 345, L51
Léger, A., & Puget, J. L. 1984, A&A, 137, L5
Livio, M. 1994, in Circumstellar Media in the Late Stages of Stellar Evolution, ed. R. Clegg, I. Stevens, & W. Meikle (Cambridge: Cambridge Univ. Press), 35
Masson, C. R. 1990, ApJ, 346, 243
Meixner, M., Skinner, C. J., Graham, J. R., Keto, E., Jernigan, J. G., & Arens, J. F. 1997, ApJ, 482, 897
Montou, C., Léger, A., & d'Hendecourt, L. 1996, A&A, 310, 297
Omont, A. 1995, ApJ, 454, 819
Savage, B. D., & Mathis, J. S. 1979, ARA&A, 17, 73
Schutte, W. A., Tielens, A. G. G. M., & Allamandola, L. J. 1993, ApJ, 415, 397
Skinner, C. J., Meixner, M. M., Hawkins, G. W., Keto, E., Jernigan, J. G., & Arens, J. F. 1994, ApJ, 423, L135
Soker, N., & Livio, M. 1989, ApJ, 339, 268
Sourisseau, C., Coddens, G., & Papoular, R. 1992, A&A, 254, L1
Spitzer, L. 1978, Physical Processes in the Interstellar Medium, (New York: Wiley)
Walmsley, C. M., Chini, R., Kreysa, E., Steppe, H., Forveille, T., & Omont, A. 1991, A&A, 248, 555
Woodsworth, A. W., Kwok, S., & Chan, S. J. 1990, A&A, 228, 503
Zuckerman, B., & Aller, J. H. 1986, ApJ, 301, 772